Holographic Simulation of Correlated Electrons on a Trapped-Ion Quantum Processor

Daoheng Niu,[1,*] Reza Haghshenas,[2,†] Yuxuan Zhang,[1] Michael Foss-Feig,[3] Garnet Kin-Lic Chan,[2] and Andrew C. Potter[4]

[1] *Department of Physics, University of Texas at Austin, Austin, Texas 78712, USA*

[2] *Division of Chemistry and Chemical Engineering, California Institute of Technology, Pasadena, California 91125, USA*

[3] *Quantinuum, 303 S Technology Ct. Broomfield, Colorado 80021, USA*

[4] *Department of Physics and Astronomy, and Stewart Blusson Quantum Matter Institute, University of British Columbia, Vancouver, British Columbia V6T 1Z1, Canada*

(Received 10 February 2022; revised 10 June 2022; accepted 5 July 2022; published 2 August 2022)

We develop holographic quantum simulation techniques to prepare correlated electronic ground states in quantum matrix-product-state (QMPS) form, using far fewer qubits than the number of orbitals represented. Our approach starts with a holographic technique to prepare a compressed approximation to electronic mean-field ground states, known as fermionic Gaussian matrix-product states (GMPSs), with a polynomial reduction in qubit and (in select cases gate) resources compared to existing techniques. Correlations are then introduced by augmenting the GMPS circuits in a variational technique, which we denote GMPS+X. We demonstrate this approach on Quantinuum's System Model H1 trapped-ion quantum processor for one-dimensional (1D) models of correlated metal and Mott-insulating states. Focusing on the 1D Fermi-Hubbard chain as a benchmark, we show that GMPS+X methods faithfully capture the physics of correlated electron states, including Mott insulators and correlated Luttinger liquid metals, using considerably fewer parameters than problem-agnostic variational circuits.

DOI: 10.1103/PRXQuantum.3.030317

As quantum computers have begun to achieve the scale and reliability required to surpass classical computations on certain theoretically contrived tasks such as random quantum circuit sampling [1–3], it is natural to ask how best to apply their computational abilities to problems of technological and scientific interest. The quantum simulation of molecules and materials is a promising target application, where there are theoretical grounds to expect exponential quantum computational advantage [4] in certain types of quantum dynamics, with prospective applications to nonequilibrium electron transport, quantum reactive scattering, and the dynamics of strongly coupled field theories. An important prerequisite to computing dynamics in physical applications is to first prepare a good approximation to the ground or thermal state of a correlated electron system. In variational approaches, a key goal is to use physically inspired circuit ansatzes to reduce the number of variational parameters and simplify the optimization landscape. Matrix-product states (MPSs) [5] provide a compact parameterization of many physically important quantum states since the memory and complexity of MPS calculations are controlled by the extent of spatial correlations and entanglement, encoded by the matrix size ("bond dimension") χ. A growing body of work [6–13] has begun to extend the efficient data compression afforded by classical MPS techniques to the quantum domain, using quantum memories with approximately $\log_2 \chi$ qubits to represent the bond space of a MPS, and quantum circuits interleaved with partial measurement to implement its tensors. By exploiting mid-circuit measurements and qubit reuse (MCMR) [7], a quantum MPS (QMPS) simulation of a d-dimensional systems can be performed with effectively $(d-1)$ dimensions' worth of qubits, earning the moniker "holographic simulation" [7,14]. Early demonstrations of holographic QMPS [6,7,9] and their higher-dimensional quantum tensor network (QTNS) generalizations [11,12] have focused on simple spin models. However, more realistic molecular and material models contain fermionic electrons, which commonly exhibit quite entangled (e.g., metallic) ground states even for weak

*daoheng@utexas.edu
†haqshena@caltech.edu

interaction strengths, and whose Hamiltonians have more complex qubit representations.

Because many correlated electron states are adiabatically connected to Gaussian (e.g., mean-field) states, we first describe how to prepare holographically Gaussian MPS (GMPS) as a QMPS. We start from a classical construction of Fishman and White [15] that naturally compresses Gaussian fermionic states in GMPS form. A key aspect of this compression is that, unlike other mean-field preparation techniques, it exploits the near-area-law nature of the ground state to parametrically reduce qubit and gate resources. We present numerical evidence that this holographic GMPS method gives a polynomial reduction in the number of qubits (and in certain cases, gates) compared to standard quantum algorithms. Next, using the one-dimensional (1D) Fermi-Hubbard chain as a benchmark, we show that augmenting the mean-field GMPS state with shallow circuits (which we refer to as GMPS+X) enables more accurate variational preparation of correlated electron ground states with far-fewer parameters than problem-agnostic ansatzes, a key component for scaling up QMPS methods to solve larger and more classically challenging models. We implement the GMPS and GMPS+X methods on Quantinuum's system model H1 trapped-ion quantum processor, demonstrating that the resource reductions enable the faithful simulation of systems with up to 16 orbitals using minimal error mitigation. Finally, we explore extending the GMPS compression to two dimensions, where we show that the required qubit resources continue to be asymptotically optimal, and discuss the potential advantages of this method for simulating correlated topological phases.

I. QUANTUM MATRIX PRODUCT STATES

Here, we briefly recap the holographic simulation with QMPS. Interested readers may find a more detailed exposition in Ref. [7]. Holographic simulation with QMPS is based on the MPS representation:

$$|\Psi\rangle = \sum_{n_1 \ldots n_L} \ell^T A^{n_1} A^{n_2} \ldots |n_1 n_2 \ldots n_L\rangle, \tag{1}$$

where $n_x \in \{1, 2, \ldots d = 2^{N_p}\}$ label the orbital occupation numbers of the N_p different physical spin or orbital "flavors" at position x, A^{n_x} is a $\chi \times \chi$ matrix for each n_x label, and ℓ is a χ-dimensional vector that determines the left-boundary conditions. Two-dimensional (2D) and three-dimensional (3D) systems can also be treated in this framework by treating the system as a 1D stack of $(d-1)$-dimensional cross sections. In this case, χ must scale exponentially in the cross-section area for area-law states.

Properties of any MPS in right-canonical form (RCF) [16] can be measured on a quantum computer by implementing its transfer matrix as a quantum channel [17] acting on $N_p = \log_2 d$ "physical" qubits and $N_b = \log_2 \chi$ bond qubits [7]. The bond vector ℓ is prepared by acting on the bond qubits plus optional ancilla with a unitary U_ℓ. Each tensor A is then embedded into a larger block unitary operator U_A acting on a reference initial state, $|0\rangle$, of the physical qubits: $A^n_{ij} = \langle n|_p \otimes \langle i|_b U_A |0\rangle_p \otimes |j\rangle_b$ where subscripts p and b, respectively, denote physical and bond qubits. Then, the physical qubits can be measured in any desired basis (without measuring the bond qubits). The process is then repeated for each site in sequence from left to right until the measurement is completed. As for any quantum algorithm, repeated statistical sampling of these measurements must be used to estimate the expectation values of observables. In this way, one can measure any product operator of the form $\prod_{x=1}^{L} \mathcal{O}_x$, which forms a complete basis for general observables. To summarize, the QMPS procedure for sampling an observable of the form $\langle\psi| \prod_{x=1}^{L} \mathcal{O}_x |\psi\rangle$ is as follows:

1. Prepare the bond qubits in a state corresponding to the left-boundary vector ℓ.
2. Reset the physical qubit for site $[x = 0]$ in a fixed reference state $|0\rangle$.
3. Perform a quantum circuit representing U_A at site $[x]$, entangling the physical and bond qubits.
4. Measure the physical qubit in the eigenbasis of O_x and weight the measurement outcome by the corresponding eigenvalue of that observable. The bond-qubit register now corresponds to bond connecting sites x and $x+1$.
5. Repeat steps 1–4 for $x = 1 \ldots L$, and discard the bond qubits [18].

Since the physical qubits for site x are reset and reused as physical qubits for site $x+1$, this QMPS procedure saves the total number of qubits to be used and enables a small quantum processor to achieve quantum simulation tasks with a bigger size than its available number of qubits. Moreover, the entanglement spectrum of the bond qubits in between sites x and $x+1$ coincides with the bipartite entanglement spectrum of the physical MPS at that entanglement cut, further enabling measurement of nonlocal entanglement observables, as recently demonstrated experimentally for near-critical spin chains [7].

II. MODELS AND OBSERVABLES

We focus on quasi-1D Fermi-Hubbard (FH) models, which we write in the form

$$H_{\mathrm{FH}} = -t \sum_{\sigma,\langle \mathbf{r},\mathbf{r}'\rangle} c^\dagger_{\mathbf{r},\sigma} c_{\mathbf{r}',\sigma} + \frac{U}{2} \sum_{\mathbf{r}} n_{\mathbf{r}} (n_{\mathbf{r}} - 1) - \mu N, \tag{2}$$

where $c^\dagger_{\mathbf{r},\sigma}$ creates an electron at site $\mathbf{r} = (x, y)$ with z component of spin $\sigma \in \{\uparrow, \downarrow\}$, $1 \le x, y \le L_{x,y}$,

$n_{\mathbf{r}} = \sum_\sigma c^\dagger_{\mathbf{r}\sigma} c_{\mathbf{r}\sigma}$, $N = \sum_{\mathbf{r}} n_{\mathbf{r}}$, t is the hopping strength, U is the onsite Hubbard interaction, and μ is the chemical potential. We measure three types of observables, single-particle equal-time Green's functions (also known as one-electron density matrices), G, and connected density-density and spin-spin correlators, C_{nn} and C_{SS}:

$$\begin{aligned} G_{\mathbf{r},\sigma;\mathbf{r}',\sigma'} &= \langle c^\dagger_{\mathbf{r},\sigma} c_{\mathbf{r}',\sigma'} \rangle, \\ C_{nn}(\mathbf{r},\mathbf{r}') &= \langle n_{\mathbf{r}} n_{\mathbf{r}'} \rangle - \langle n_{\mathbf{r}} \rangle \langle n_{\mathbf{r}'} \rangle, \\ C_{SS}(\mathbf{r},\mathbf{r}') &= \langle S^z_{\mathbf{r}} S^z_{\mathbf{r}'} \rangle - \langle S^z_{\mathbf{r}} \rangle \langle S^z_{\mathbf{r}'} \rangle, \end{aligned} \tag{3}$$

where $S^z_{\mathbf{r}} = 1/2 \sum_{\sigma,\sigma'} c^\dagger_{\mathbf{r},\sigma} \sigma^z_{\sigma\sigma'} c_{\mathbf{r},\sigma'}$.

To simulate fermionic systems, one needs to encode the physical fermionic orbital creation and annihilation operators into bosonic qubit degrees of freedom. A variety of encodings are available. Throughout this work, we adopt the Jordan-Wigner (JW) encoding, which is natural for quasi-1D settings, with the convention that orbitals are ordered first by spin $\{\uparrow,\downarrow\}$, then by ascending y position, and finally by ascending x position. We remark that the holographic representation in principle enables (Appendix F) one to reduce the maximal length of JW strings that one needs to measure in variational calculations from approximately $L^d \to L^{d-1}$, reducing the impact of measurement errors in computing long-distance correlation functions.

III. COMPRESSING GAUSSIAN STATES AS QMPS

We begin by briefly reviewing the classical MPS algorithm to construct a MPS representation of Gaussian fermion states, and explain how to recast the resulting GMPS as a QMPS.

A. Compressed Gaussian MPS

The ground state of a noninteracting fermion Hamiltonian with N_o orbitals: $H = \sum_{i,j=1}^{N_o} c_i^\dagger h_{ij} c_j$ is fully characterized by its $N_o \times N_o$ single-particle Green's function: $G_{ij} = \langle c_i^\dagger c_j \rangle$ (generalizations to non-number conserving Hamiltonians are discussed in Appendix E), which has highly degenerate eigenvalues of either 0 or 1 and whose eigenvectors correspond to unoccupied or occupied orbitals, respectively. Green's function is preserved by any unitary transformation acting separately on the (un)occupied subspaces. The compression scheme of Ref. [15] exploits this freedom by progressively disentangling well-localized degrees of freedom in blocks of B adjacent sites, where B is chosen to be sufficiently large to achieve target infidelity, ϵ. Starting with the upper-left $B \times B$ block of G, one finds the eigenvector of this sub-block whose eigenvalue is closest to either 0 or 1 and performs a series of 2×2 (single-particle) unitary rotations that move this eigenvector to the first site of the block. The procedure is iterated for the remaining $(N_o - 1) \times (N_o - 1)$ sites until Green's function is approximately diagonalized.

The composition of all the basis rotations in the above procedure produces an $N_o \times N_o$ unitary, $u^\dagger = (\prod_{\alpha=1}^{(B-1)(N_o - B/2)} u_\alpha)^\dagger$, consisting of a ladder of 2×2 single-particle unitaries labeled by ordered index α, which approximately diagonalizes the Green's function. Alternatively, read in reverse, the inverse transformation u approximately converts a product state of (un)occupied sites into the entangled ground state of h. These single-particle (size $n \times n$) operations can be converted into a circuit acting on the many-particle Hilbert space (of size 2^n) by replacing each 2×2 unitary, u_α, by an equivalent two-qubit gate:

$$U_\alpha = \exp\left[\sum_{ij} c_i^\dagger (\log u)_{ij} c_j\right] = \exp\left[\sum_{ij} \sigma_i^+ (\log u)_{ij} \sigma_j^-\right],$$

where in the second line we use the fact that the rotation always occurs between neighboring sites and therefore does not involve a Jordan-Wigner string.

Crucially, the resulting ladder circuit $U = \prod_\alpha U_\alpha$ can be interpreted as a QMPS with bond dimension $\chi = 2^B$ by chopping it into diagonal causal slices (see Fig. 1), and interpreting the qubit lines entering the bottom of the slice as physical qubits and those entering the side as bond qubits. We refer to the resulting MPS as a GMPS to distinguish it from generic non-Gaussian (Q)MPS of the same bond dimension.

Whereas an arbitrary Gaussian state can be prepared by a ladder circuit acting on N_o qubits with $O(N_o^2)$ two-qubit gates (see, for example, Refs. [19,20]), the compressed GMPS *ground state* requires $O(N_o B)$ two-qubit gates acting on $O(B)$ qubits (if implemented holographically). The efficiency of this compression, therefore, depends on the block size B required to accurately approximate the state in question. Empirical numerical evidence and entanglement-based arguments indicate that GMPS for ground states of local Hamiltonians in 1D systems of length L and for target error threshold $\epsilon = 1 - 1/L \sum_{i,j} |G_{ij}^{(\mathrm{GMPS})} - G_{ij}|$ requires block size (equivalently number of qubits) $B \sim \log \epsilon^{-1}$ for a gapped state or $B \sim \log L \log \epsilon^{-1}$ for a gapless metallic state. In Sec. V below, we extend these results to 2D systems, and find that generically B scales with the bipartite entanglement entropy $S(L)$:

$$B \sim S(L) \sim \begin{cases} L \log \epsilon^{-1} & \text{gapped} \\ L \log L \log \epsilon^{-1} & \text{Fermi surface} \end{cases} \tag{4}$$

[21]. We conjecture that similar scalings with $L \to L^2$ hold in 3D (e.g., this follows straightforwardly from the 1D results for translation-invariant systems). This result holds even for topologically nontrivial Chern band insulators that have an obstruction to forming a fully localized

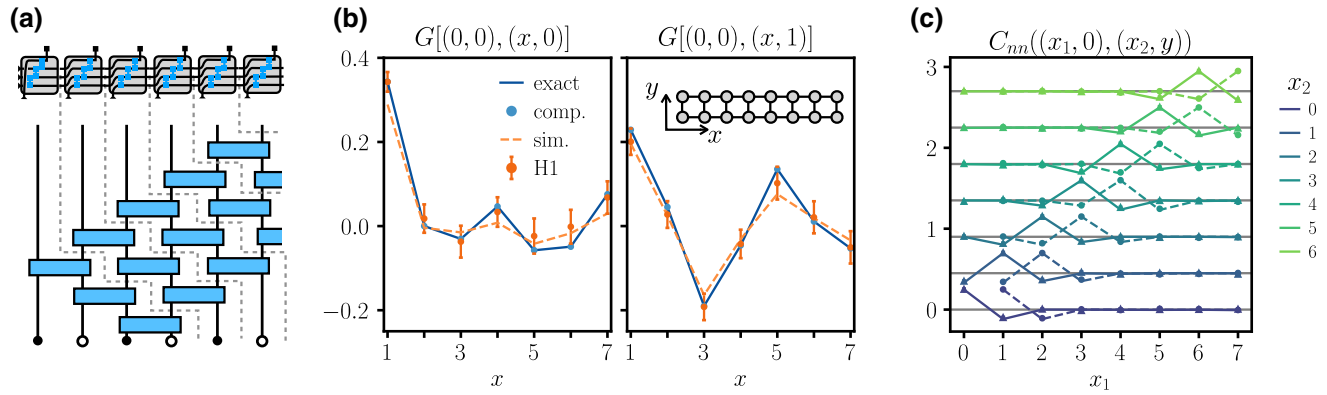

FIG. 1. Compressing Gaussian fermion states as QMPS—(a) holographic QMPS implementation (top) of the GMPS circuit (bottom) for approximately preparing compressed Gaussian fermion states. (b)–(c) Experimental implementation of holographic GMPS algorithm for a spinless two-leg ladder at half-filling. (b) (Real part of) Green's function, Re $G\left[\mathbf{r}=(0,0),\mathbf{r}'=(x,y)\right]$ with experimental data (orange dots with 1σ error bars from 1000 measurement shots per point), noisy circuit simulations with one-qubit and two-qubit gate depolarizing parameters $p_{1q}=10^{-3}$ and $p_{2q}=5\times10^{-3}$, respectively (dashed orange line), and exact values (solid blue line). (c) Connected part of density-density correlators $C_{nn}(\mathbf{r},\mathbf{r}')$ with $\mathbf{r}=(x_1,0)$ and $\mathbf{r}'=(x_2,y)$, with $y=0$ data shown as solid lines (theory) and triangles (experiment), and $y=1$ data shown as dashed lines (theory) and circles (experiment), respectively. Each point represents 5600 measurement shots. Statistical error bars in (c) are included, but smaller than plot symbols.

Wannier basis. Combined with holographic simulation methods using mid-circuit measurement and reuse, this method dramatically reduces the number of qubits required ($L^{d-1}B$ versus L^d) to implement the GMPS on a quantum computer.

B. Trapped-ion GMPS implementation

To demonstrate the feasibility of this approach for near-term hardware, we prepare an entangled metallic ground state of a spinless noninteracting two-leg ladder described by Eq. (2) without spin, and with $L_x=8, L_y=2, U=0$, and $N=8$ electrons (half-filling). This system has the same number of degrees of freedom of a spinful $L_x=8$ FH chain that we are ultimately interested in, but avoids the trivial decoupling of spin species that arises in mean-field ground states of the FH chain. The QMPS representation of the compressed GMPS is implemented on Quantinuum's System Model H1 trapped-ion quantum computer utilizing six trapped-ion qubits corresponding to block size $B=2\times3$, sufficient to reduce the theoretical compression error below 1%. Using only a simple error-mitigation scheme based on postselecting data with the correct total electron number (see Appendix D for details), we achieve close to a quantitative agreement (within statistical error bars) between the experimental correlation functions and their theoretical values (see Fig. 1).

IV. CORRELATED ELECTRON MODELS

Since noninteracting fermion systems permit efficient classical simulation, the GMPS technique is not directly useful on its own. However, holographic QMPS approximations to mean-field states can be helpful starting points for approximating correlated ground states either by (i) adiabatic evolution to a correlated system in the same phase as the mean-field state (using efficient holographic time-evolution methods [7]), or (ii) reducing the complexity of variational state preparation by providing a good initial guess. Here, we focus on the variational approach (ii) and show that relatively simple variational-circuit extensions of the GMPS circuit, which we refer to as GMPS+X methods, provide good approximations to interacting fermion ground states of a spinful FH chain [Eq. (2) with $L_y=1$]. Since this model can be exactly solved by Bethe-Ansatz methods, it provides a convenient, high-precision benchmark of these techniques. We implement two different GMPS+X ansatzes, which we refer to as GMPS+J and GMPS+U, respectively, and compare their performance against a problem-agnostic ansatz where the QMPS tensors are generated by a brickwork circuit of general (number-conserving) two-qubit gates. In each of the GMPS+X approaches, we first construct a GMPS circuit corresponding to the Hartree-Fock (HF) ground state. At half-filling ($\nu=1/2$, one electron per site), the HF ground state has antiferromagnetic (AFM) order with order parameter: $\mathcal{N}=\sum_j(-1)^j\langle S_j^z\rangle\neq0$. The long-range AFM order is, of course, an artifact of the HF approximation, and the true ground state has only power-law decaying AFM correlations due to strong quantum fluctuations. We also consider one-third-filling ($\nu=1/3$, two electrons per three sites), where we use a HF ground-state solution that is a nonmagnetic Fermi gas, and the true ground state is a correlated Luttinger liquid with spin-charge separation.

A. Variational ansatzes

Here we introduce and briefly describe the different variational approaches considered (see Fig. 2), and compare their performance through numerical simulations. Additional details on the construction and implementation of circuits for each ansatz can be found in Appendix C.

a. GMPS+J ansatz The GMPS+J ansatz is specific to half-filling ($\nu = 1/2$), where the charge degrees of freedom are gapped, and the low-energy fluctuations of the FH chain are approximately described by a Heisenberg spin-1/2 chain. Roughly speaking, we can think of the GMPS circuit as transforming from the sites of a spin-1/2 chain to the Wannier orbitals for the Mott-insulating FH chain. With this picture in mind, we can build in spin correlations by adding variational layers *before* the GMPS circuit, such that the GMPS circuit produces an entangled state of the Wannier-orbital spins, rather than a simple Neél product state [Fig. 2(a)]. Specifically, we choose a single variational circuit layer that is equivalent (up to a basis change) to that used in Ref. [7] to approximate the Heisenberg spin-chain ground state as a QMPS using a single bond qubit (see Appendix C for details). We see that this ansatz performs best at half-filling and large U, where the FH chain can be well approximated by a spin chain. The chief advantage of this ansatz is that it is very compact, requiring only a single variational parameter per site.

b. GMPS+U ansatz The GMPS+U ansatz [Fig. 2(b)] simply augments each of the Gaussian fermion gates in the GMPS circuit with a non-Gaussian gate $e^{-i/2(\theta_i Z\otimes Z+\alpha_i Z\otimes 1+\beta_i 1\otimes Z)}$ with variational parameters $\{\theta_i, \alpha_i, \beta_i\}$ chosen independently for each GMPS gate, i. These non-Gaussian operations make the GMPS+U gates into a general number-conserving gate (with some parameters fixed by the GMPS representation of the HF state). We see that this ansatz is more flexible than the GMPS+J method, and can achieve reasonable results over a broad range of fillings and interaction strengths, albeit at the cost of introducing additional variational parameters $n_{\text{var}} = 3N_S(B-1)$, where $N_S = 2$ denotes the number of spin components. We show that this also implies that the representational power of the GMPS+U ansatz increases with B, and give evidence that this enables the ansatz to be scaled to achieve the arbitrary desired variational accuracy (Fig. 4).

c. Brick QMPS ansatz Finally, we compare the GMPS + U approaches to a problem-agnostic QMPS whose tensors are generated by a brickwork circuit [see Fig. 2(c)] of arbitrary (charge-conserving) two-qubit gates. In this approach, the circuit parameters are not constrained except by symmetry. Specifically, we enforce charge conservation by demanding the circuits commute with the total S^z of the physical and bond qubits, resulting in five variational parameters per gate [22].

B. Comparison of variational approaches

Figure 3 shows numerical results for the relative error $\epsilon = (E - E_{\text{exact}})/|E_{\text{exact}}|$ between the variational energy E,

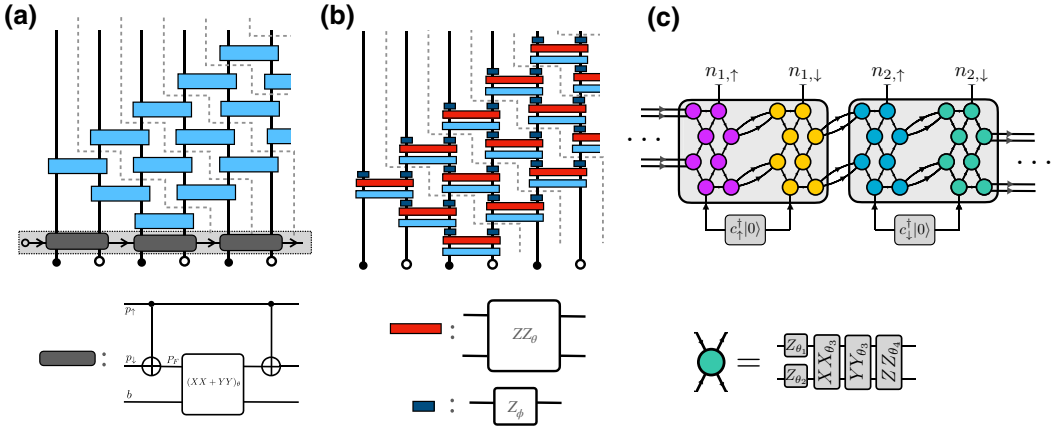

FIG. 2. Variational circuit architectures for correlated electron problems—the GMPS+X approaches augment the GMPS circuit preparing the Hartree-Fock ground state with non-Gaussian gates that build in correlations either by (a) GMPS+J: introducing an extra QMPS layer with an extra bond qubit (gray dashed box) or by (b) GMPS+U: generalizing the GMPS gates (blue boxes) to include non-Gaussian operations, $ZZ_\theta = e^{-\frac{i}{2}\theta Z\otimes Z}$ and $Z_\phi = e^{-\frac{i}{2}\phi Z}$. Here we draw the GMPS+X circuits only for block size $B = 3$ (the implemented circuits have twice this block size, $B = 6$ to include spin). (c) A problem-agnostic brick QMPS ansatz consisting of a brickwork of general number-conserving two-qubit gates. Here, for any Hermitian operator O, O_θ denotes a gate corresponding to unitary $u[O_\theta] = e^{-i\theta O/2}$.

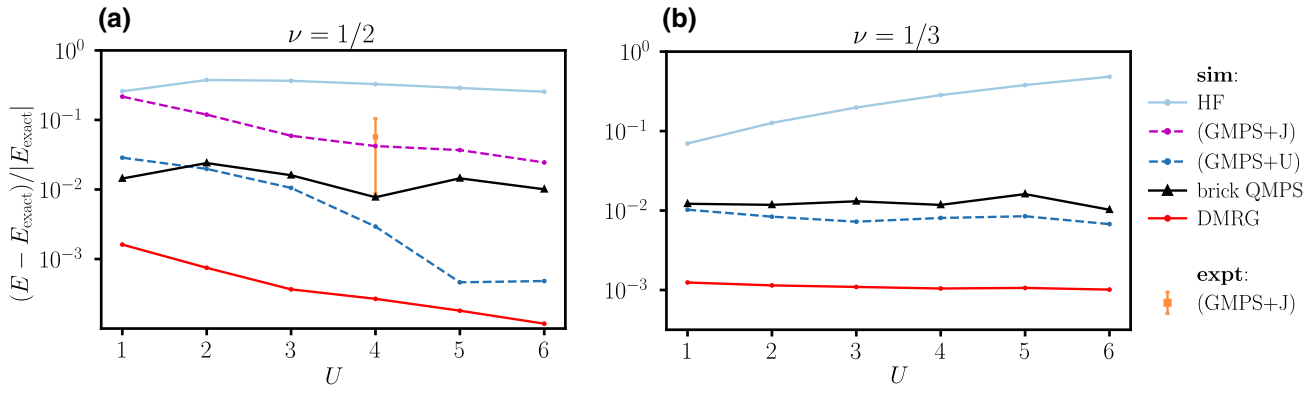

FIG. 3. Comparison of variational approaches to the Fermi-Hubbard chain—relative error in energy of (a) half-filling (b) (1/3)-filling Fermi-Hubbard chain for various variational approaches compared to the exact ground state of the corresponding Fermi-Hubbard chain. Variational approaches include two types of GMPS+X circuits: GMPS + J and GMPS + U that augment the GMPS with $B = 6$ for the Hartree-Fock ground state with additional variational circuitry, and a problem-agnostic QMPS ansatz with two bond qubits and four layers of brick circuit (brick QMPS) (see Appendix B for details of circuit ansatzes). The GMPS+U simulations are performed for an $L = 18$ site chain, whereas the brick QMPS and DMRG calculations are performed for an infinite chain. For comparison to classical methods, we include the mean-field (MF) solution, and DMRG results with bond dimension 2^5 that provide a lower bound on the achievable energy with $n_b = 5$ bond qubits ($n_b = B - 1$ in general) used in the GMPS+U approach. The number of variational parameters per (spinful) site are, respectively, 1 (GMPS+J), 30 (GMPS+U), 80 (brick QMPS), and 1024 (DMRG with $\chi = 2^5$).

and the exact ground-state energy E_{exact}, for different variational QMPS ansatzes at fillings $\nu = 1/2, 1/3$ and various interaction strengths $1 \leq U \leq 6$. These are additionally compared to the HF approximation and a classical density matrix renormalization group (DMRG) calculation with bond dimension $\chi = 2^5$, equivalent to the bond dimension for the $n_b = 5$ bond qubits needed for the GMPS+X approaches. Since DMRG effectively converges to near-optimal results in these types of simple 1D problems, the DMRG calculation can be viewed as an effective lower bound on the performance of variational circuit ansatzes with $n_b \leq 5$ bond qubits. We note that, while the DMRG energy error is significantly lower than the variational QMPS results in this example, (i) this relies crucially on the tractability of 1D DMRG calculations, which does not extend to more complicated problems in 2D, and (ii) we show that the GMPS+U method can be readily scaled to achieve comparable accuracy with far-fewer variational parameters (see Fig. 4).

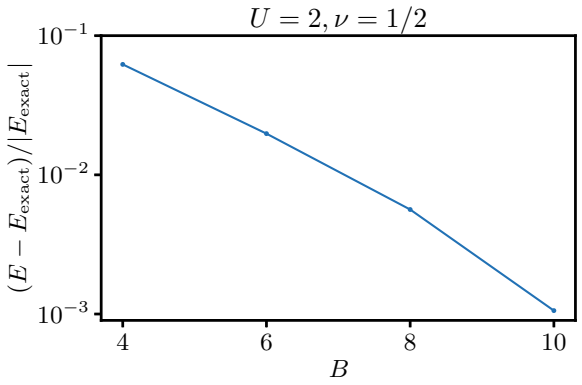

FIG. 4. Scaling of the GMPS+U method when changing block size B—variational energy of GMPS+U ansatz for the Fermi-Hubbard chain at half-filling with $U = 2$ converges rapidly (approximately exponentially over the range of parameters explored) with block size B, which suggests that this method can be used to achieve the arbitrary desired accuracy.

To obtain a scalable variational ansatz, it is critical to reduce the number of variational parameters per site, n_{var}, required to achieve a desired accuracy. Optimizing complex variational circuits with large n_{var} is generically a classically difficult (nonlinear, nonconvex, and high-dimensional) problem and creates significant sampling overhead for measuring energies and gradients on quantum devices. The complexity of the ansatzes ranges from $n_{\text{var}} = 1$ for GMPS+J, $n_{\text{var}} = 24$ for GMPS+U, and $n_{\text{var}} = 80$ for the brick QMPS, to $n_{\text{var}} = \chi^2 = 1024$ for DMRG. We note that, while we present simulation results for a finite number ($L = 18$) of spinful sites, the algorithm complexity presented scales (empirically) efficiently in L, and for the parameters explored this L is sufficiently large to accurately capture the thermodynamic limit (see Fig. 5).

In general, we observe that the GMPS+X techniques offer a significant reduction in the number of variational parameters n_{var} required to achieve a given accuracy. At $\nu = 1/2$, the simplest ansatz, GMPS+J already achieves significant improvement over the mean-field results despite its extreme simplicity. Moreover, the GMPS+U ansatz outperforms the brick QMPS variational circuits across the entire

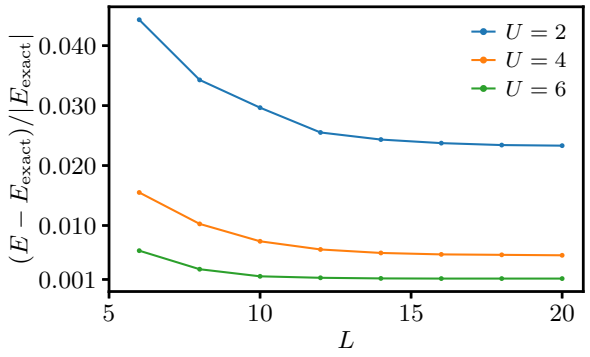

FIG. 5. Scaling of the GMPS+U ethod when changing system size L—the relative error in energy versus the total length L of spinful sites for the FH model at $U = 2, 4, 6$ and $\nu = \frac{1}{2}$ and fixed block size $B = 6$.

ν, U parameter space explored, despite having significantly lower n_{var}.

The GMPS+U ansatz can be scaled to achieve higher accuracy by changing the block size B (which also adjusts the number of variational parameters for building in correlations). Empirically, in the range of B explored, we find that this allows one to adjust the complexity of the ansatz to achieve a desired target error rate. To explore the scalability, we focus on the weak Mott-insulating regime ($U = 2$, $\nu = 1/2$) where the GMPS+U error in Fig. 2 is large, yet interactions are still important. Here, we observe a rapid decay of error with block size, that follows an approximately exponential trend $\epsilon \sim e^{-cB}$ with $c \approx 0.7$ over the range of B explored. We note that the mean-field GMPS compression error is already very low at $B = 4$, and attribute the improvement with B to the more flexible variational ansatz better capturing multiparticle correlations. At the largest block sizes, $B = 10$, the GMPS+U technique achieves performance equal to the classical $\chi = 32$ DMRG despite having over an order of magnitude fewer variational parameters ($n_{\text{var}} = 54$ versus 1024). These results show that the GMPS+U approach can achieve high precision and scalable performance for simulating strongly correlated electron models with far-fewer variational parameters than problem-agnostic circuit ansatzes.

C. Trapped-ion GMPS+X d emonstration

We implement the simplest extended GMPS version, the GMPS+J variational ansatz, in the Quantinuum system model H1 trapped-ion quantum processor, focusing on the specific case of $\nu = 1/2$ and intermediate interaction strength ($U = 4$), and for a Fermi-Hubbard chain of length $L = 6$. To avoid the lengthy process of hybrid classical quantum optimization, we perform the optimization through classical simulation, and simply implement the classically optimized circuit in hardware. We employ a simple error-mitigation technique of postselecting data on having the correct total number of particles (see Appendix D for details).

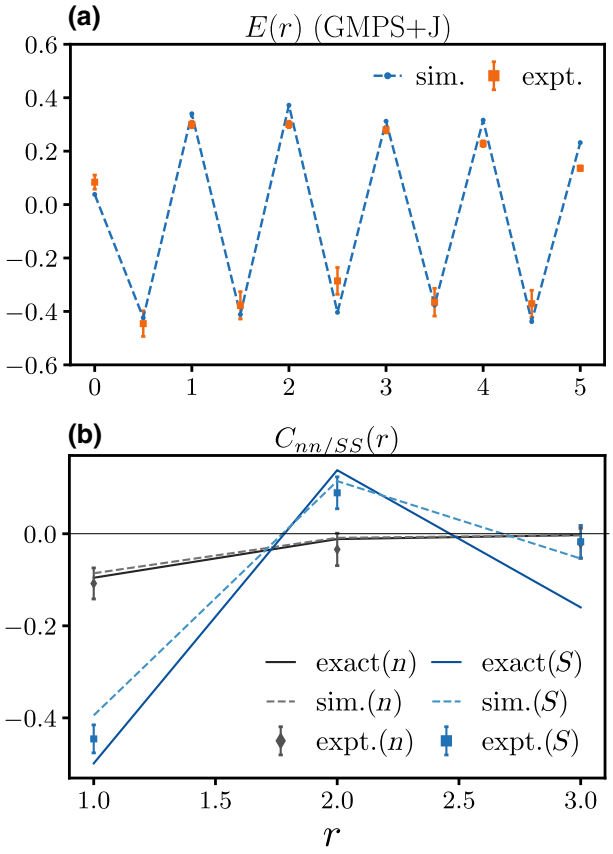

FIG. 6. GMPS+J hardware implementation—for the Fermi-Hubbard chain at half-filling with $U = 4$. (a) Energy density versus position in the GMPS+J ansatz (which is not explicitly translation invariant), with hopping energies shown at half-integer (bond-centered) positions. (b) Connected spin (S) and charge density (n) correlators show spin-charge separation with rapid decay of charge and slower (antiferromagnetically modulated) decay of spin correlations.

Figures 6(a) and 6(b), respectively, show the energy densities (for each bond) and correlation functions for a chain of length $L = 6$. Comparing to ideal (noiseless) circuit simulations, and exact (Bethe-ansatz) results, we find a good quantitive agreement to the experimental results within the statistical error bars from a finite shot rate of between 400 and 1000 shots per data point (see Table I for details on the number of measurement shots, including error-mitigation postselection). In addition to the quantitative agreement, the correlation data shows a clear separation of spin and charge with rapidly decaying charge correlations and longer-range spin correlations.

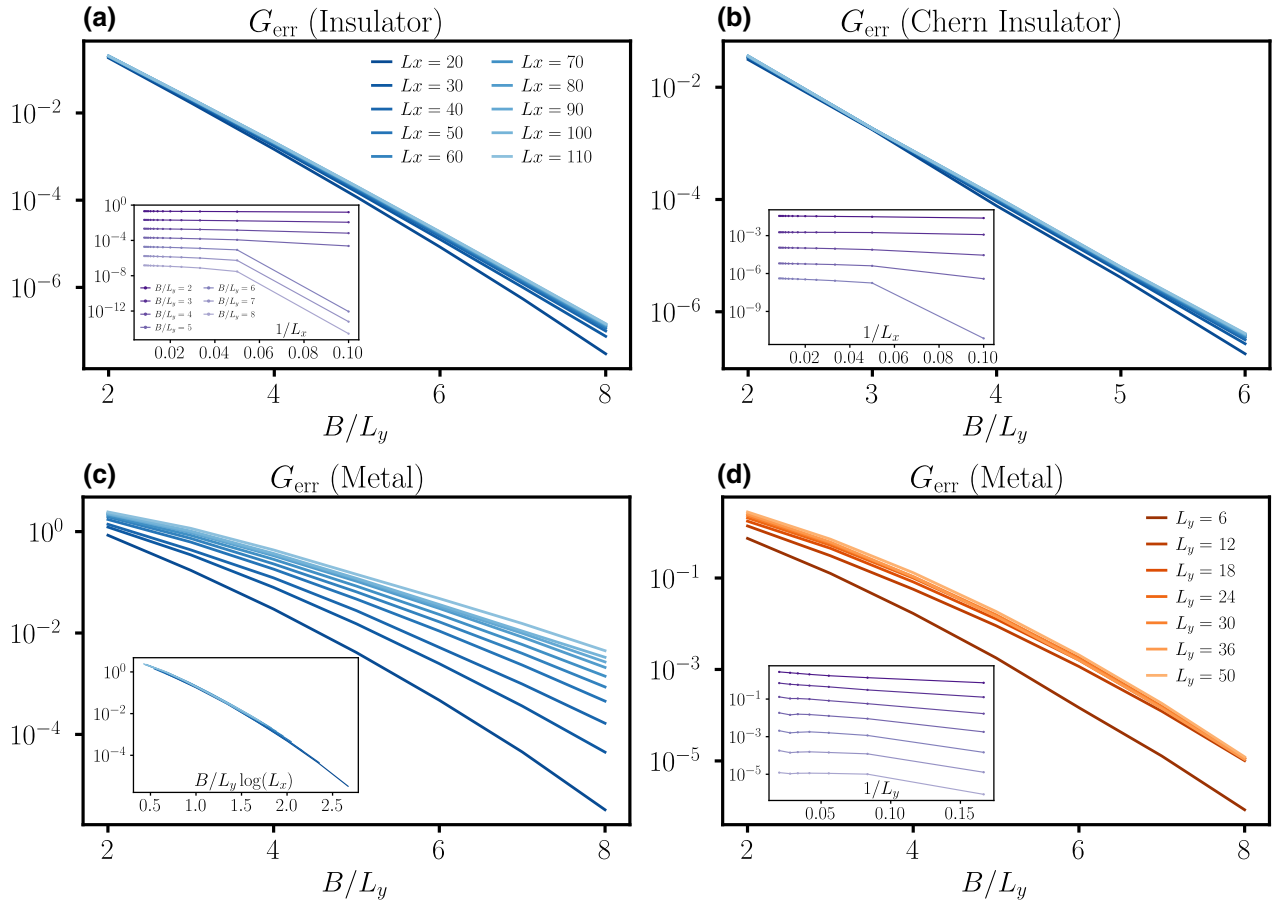

FIG. 7. GMPS compression resource scaling: (a)–(d) show the mean error $G_{\rm err}$ of Green's functions versus the GMPS compression block size for various systems and system sizes. $G_{\rm err}$ is defined by $G_{\rm err} = \sum_{i,j} |G^c_{i,j} - G^o_{i,j}|/V$, where G^o and G^c are the original and compressed Green's function and V is the system size. In each plot we stop at the block size when the eigenvalues cannot be improved by increasing block size as it already reaches the limit of machine precision 10^{-15}. (a)–(c) show the error versus the block sizes for different L_x while L_y is fixed (to 1,6,6); (d) shows the compression error versus the block sizes for different L_y with $L_x = 50$. The insets of (a),(b),(d) show the $G_{\rm err}$ versus $1/L_x$ or $1/L_y$. The inset of (c) shows the $G_{\rm err}$ versus the block size rescaled by $\log(L_x)$.

V. RESOURCE SCALING OF GMPS COMPRESSION IN 2D

While the GMPS method was originally developed for 1D systems, one can straightforwardly extend it to higher dimensions, by adopting an approach similar to that of 2D DMRG where a 2D system of length L_x and width L_y is considered as a stack of L_x "slices," or similarly by treating a 3D system as a stack of 2D cross sections. Focusing on 2D (we expect similar results to hold in 3D), we empirically investigate the resource scaling required to implement GMPS representations of three important classes of states (see Fig. 7):

1. A topologically trivial 1D band insulator (L_y=1) is constructed from the Su-Schreifer-Heeger (SSH) model with Hamiltonian $H_{\rm SSH} = -t\sum_{j=1}^{N-1} \left(1 + (-1)^j \delta\right) c_j^\dagger c_{j+1} + h.c.$ with $\delta = 1/2$.
2. A topologically nontrivial Chern insulator is constructed from the ground state of a square lattice π-flux tight-binding model of Ref. [23], with parameters t_1=1, t_2=1, and the periodic boundary condition in L_y direction (to avoid gapless chiral edge states along the cylinder).
3. A two-dimensional metal with a Fermi surface from an isotropic tight binding is constructed from the ground state of a square lattice tight-binding Hamiltonian $H = \sum_{\langle i,j\rangle}(-tc_i^\dagger c_j + \text{h.c.})$ where $\langle\rangle$ denotes the neighboring sites, with the periodic boundary condition in L_y direction.

We measure the quality of the GMPS approximation via the mean error in the entries of G_{ij} and focus on the regime where the eigenvalues obtained in the GMPS approximation can be improved until machine precision by using larger block sizes. In each case, we provide numerical

evidence that the block size required for the GMPS compression scheme follows that expected by the entanglement structure of these states, namely to achieve error ϵ requires $B \sim L_y \log(1/\epsilon)$ for both topological and trivial insulating states, and $B \sim L_y \log L_x \log(1/\epsilon)$ for metals, which is consistent with $B \sim S(L_x, L_y)$, where $S(L_x, L_y)$ is the half-system bipartite entanglement entropy.

The Chern insulator result may initially seem surprising since the nonzero Chern number provides a fundamental obstruction to forming a localized Wannier basis, and at first glance, the GMPS algorithm may appear to be constructing such a basis. However, we note two points. First, the quasi-1D GMPS circuit structure only has locality along x, whereas the Chern obstruction forbids only simultaneous localization in both x and y directions. Specifically, the projection of the spatial coordinate into the orbitals of a Chern band $(\hat{X}, \hat{Y})$ fails to commute $[X, Y] \sim C$ where C is the Chern number. Second, we see the GMPS circuit with $B \sim \log L_x$ is accurate even for metals with Fermi surfaces where the Wannier orbitals have algebraic decay in space. This indicates that the GMPS circuit *cannot* simply be understood as a mapping to a strictly local Wannier basis. Technically, the unitary basis transformation implemented by the GMPS circuit is an upper triangular matrix and can produce long-range tails in the later entries.

One significant consequence of this result is that it implies a polynomial advantage of QMPS techniques for simulating correlated Chern insulators compared to standard quantum simulation protocols (e.g., using adiabatic state preparation). Assuming that the numerically established trends shown in Fig. 7 hold, then by leveraging (i) standard rigorous results about adiabatic evolution [24] and trotterizing continuous time evolution into circuit evolution [25,26], and (ii) previously analyzed [7] and experimentally feasible [10] methods for holographically implementing time evolution, we can establish an upper bound on the qubit and gate resources required to prepare a correlated Chern insulator (CI). Specifically, the number of gates required to prepare a noninteracting CI ground state via the GMPS method is $g \sim BL_x \sim L_y L_x \sim L^2$. Further, any correlated CI with integer Chern number is adiabatically connected to the noninteracting limit, and hence can be reached with constant-depth local time evolution, that can be implemented with constant qubit overhead via holographic time evolution [7]. This GMPS+adiabatic-preparation approach has no free variational parameters and hence this performance bound does not rely on any assumption about the efficiency of optimizing variational circuits. By contrast, adiabatic state preparation of the Chern insulator from an unentangled product state would inevitably require crossing through a phase transition since the product state and Chern insulator are topologically distinct phases (here we assume that the adiabatic evolution is performed with a local Hamiltonian). If this phase transition is continuous (second order) with dynamical critical exponent z, then the minimal gap is $\Delta \sim 1/L^z$, which requires gate count approximately $L^2/\Delta^2 \sim L^{2+2z}$. For physical transitions, $z \geq 1$, which places a bound $g \sim L^4$ for standard adiabatic preparation. Crossing a first-order transition would require much longer (exponential-in-L) adiabatic time.

Lastly, we remark that while we focus on 2D systems here, going to higher dimensions does not add any qualitatively new ingredients, and we expect the trend to continue in 3D, i.e., that the number of qubits in the GMPS continues to scale like the bipartite entanglement through a cross-section slice in all dimensions. For example, we can trivially confirm this expectation for the special case of translationally invariant systems with periodic boundary conditions in x, y and arbitrary boundary conditions in z, which can be reduced to a decoupled set of approximately $L_x L_y$ 1D systems along z for each k_x, k_y, each of which can be compressed into a GMPS with a constant (gapped systems) or approximately $\log L_z$ scaling of qubits (metals).

VI. DISCUSSION

In this work, we introduced and experimentally demonstrated holographic approaches to prepare ground states of correlated electron systems. The efficient preparation of gapped and gapless mean-field ground states as QMPS (obtained by our QMPS adaptation of the GMPS compression scheme of Fishman and White), in conjunction with holographic time-evolution algorithms [7], formally establishes that QMPS with efficient circuit resources (i.e., scaling polynomially with system size) can accurately capture any state that is continuously connected to a mean-field fermion state (possibly via a continuous phase transition). This includes most phases of matter relevant to practical material simulations, such as metals, correlated trivial and topological insulators, magnets, superconductors, density-wave states, etc.

Compared to standard adiabatic state-preparation protocols, the combination of the holographic approach, QMPS encoding, and Gaussian compression bring important advantages that are already apparent in the mean-field state preparation. For example, for gapped Hamiltonians, the holographic QMPS encoding offers a polynomial reduction in qubit resources (from $q \sim L^d$ to $q \sim L^{d-1}$), and for 2D topological systems with nontrivial Chern number further allows a polynomial reduction in gate count (from $g \sim L^4$ to $g \sim L^2$) [27]. Similarly, compared to the Givens rotation approach used in recent hardware demonstrations of Hartree-Fock ground-state preparation [20], which required $q \sim L$ qubits and $g \sim L^2$ gates, QMPS constructed via GMPS compression require only $q \sim \log L \log \epsilon^{-1}$ and $g \sim L \log L \log \epsilon^{-1}$, achieving a polynomial reduction in both resources [28]. Previously, the

most efficient Gaussian state-preparation protocol was the fermionic fast Fourier transform (FFFT), which similarly uses $g \sim L \log L$ [29] gates; however, unlike the GMPS technique, the FFFT is restricted to translation-invariant (plane-wave-like) states and requires long-range gates that spoil the holographic savings in qubit number (and may be costly to implement in many architectures). The source of the efficiency of Gaussian compression is the exploitation of the near-area-law entanglement behavior of physical gapped and gapless ground states. Retaining this structure in the QMPS then allows for compact preparation of near-area-law interacting ground states. We demonstrate this here by preparing ground states of interacting 1D fermion Hamiltonians, including those with extended power-law ground-state correlations in G_{ij}, using GMPS+X circuits adapted from the mean-field circuits.

Natural targets for follow-on work include tackling higher-dimensional systems via 2D or 3D QMPS or QTNS techniques, exploring alternative fermion-to-qubit encodings that are well suited to QTNS methods, and exploring QTNS-based embedding techniques [30] to simulate realistic material models with complex (e.g., long-range) interactions.

Given the importance of noise and errors in near-term implementations, it will further be important to systematically assess the impact of gate errors on GMPS-based circuit ansatzes. For example, related work on holographic multiscale entanglement renormalization ansatzes (MERA) suggests that holographic algorithms possess an intrinsic degree of noise resilience [31]. For QMPS circuits describing gapped 1D systems, one expects a spectral gap in the MPS transfer matrix, such that perturbing the circuits weakly with gate errors, would lead to a small, finite correction to the QMPS steady-state properties even in the limit of infinitely long systems ($L \to \infty$). Exploring the systematic dependence of this noise susceptibility for different physical types of states is a potentially interesting target for future work, and the analytic tractability of free-fermion systems may provide a tractable set of examples to explore the systematic dependence of noise sensitivity of QMPS based on the entanglement structure of the ground state being approximated.

ACKNOWLEDGMENTS

We thank Itamar Kimchi, Roger Mong, and Michael Zaletel for insightful conversations. We acknowledge support from NSF Award No. DMR-2038032 (Y.Z., A.P.), NSF-Converence Accelerator Track C award DMR- (D.N., G.K.C.), from the Alfred P. Sloan Foundation through a Sloan Research Fellowship (A.P.). R.H. was supported by the U.S. Department of Energy, Office of Science, via Award No. DE-SC0019374. Additional support for G.K.C. was provided by the Simons Collaboration on the Many-electron Problem and the Simons Investigatorship. This research was undertaken thanks, in part, to funding from the Max Planck-UBC-UTokyo Center for Quantum Materials and the Canada First Research Excellence Fund, Quantum Materials and Future Technologies Program. Numerical calculations were performed using supercomputing resources at the Texas Advanced Computing Center (TACC).

APPENDIX A: QUANTINUUM QCCD ARCHITECTURE

Hardware implementations are performed on Quantinuum's System Model H1 trapped-ion quantum processor [32], which uses a quantum charge-coupled device (QCCD) architecture, based on a Quantinuum-fabricated planar chip trap operating with three parallel gate zones and ten qubit ions. One-qubit ($1q$) gates implement $\pi/2$ rotations about an arbitrary axis in the σ^{xy} plane. The native entangling two-qubit gate is a Mølmer-Sørensen gate wrapped with single-qubit dressing pulses to achieve a phase-insensitive operation $u_{\mathrm{MS}} = \exp[-i\frac{\pi}{4} Z \otimes Z]$ [32]. The one-qubit gates and two-qubit gates have typical average infidelities (determined by randomized benchmarking techniques) of $\epsilon_{1q} \approx 10^{-4}$ and $\epsilon_{2q} \approx 2 - 5 \times 10^{-3}$.

Due to the large sampling overhead and relatively low clock speed of the QCCD device, we chose to perform only part of the holographic variational quantum eigensolver algorithms on the quantum device. Namely, in all cases, we performed the variational optimization of circuit parameters through classical simulations and implemented only the optimized circuit in hardware. While this procedure does not address the effect of hardware noise on the variational optimization (nor allow for possible variational cancellation of coherent errors), it nevertheless allows one to test how realistic hardware errors affect the achievable variational errors with different circuit types.

APPENDIX B: DETAILS OF GMPS CIRCUIT IMPLEMENTATIONS

In the GMPS compression algorithm, a basis transformation specified from the eigenvector of the Green's function block transfers the least entangled states to the first site of the block. The corresponding basis transformation is decomposed into a series of nearest-neighbor two-site gates, which rotate the Green's function block into the occupation basis. The circuit and gate parameters are obtained from the eigenvectors.

Rotating the first site to the eigenvector $(v_1, v_2, \ldots, v_{B-1}, v_B)$ requires $(B-1)$ two-site gates in total. The first gate acts on site $(B-1, B)$ and is labeled as V_{B-1}. V_{B-1} satisfies $v^T V_{B-1} = (v_1, \ldots v'_{B-1}, 0)$. In general the gate V_i satisfies $(v_1, \ldots v'_{i+1}, 0, \ldots 0)^T V_i = (v_1, \ldots, v'_i, 0, \ldots 0)$ and it takes

the form:

$$V_i = V(\theta_i) = \begin{pmatrix} \cos\theta_i & -\sin\theta_i \exp(i\phi_i) \\ \sin\theta_i \exp(-i\phi_i) & \cos\theta_i \end{pmatrix}. \tag{B1}$$

When Green's function is real, $\phi = 0$ and $\theta_{B-1} = \tan^{-1}(v_B/v_{B-1})$, thus the gate V_i takes the same form as in Ref. [15] When Green's function is complex in certain cases (like in Chern insulators), the eigenvectors are also complex thus the extra phase factor ϕ becomes necessary. The entries of Green's function are updated once the gate acts on it. The next gate acts on $(B-2, B-1)$ and so on. This procedure gives us V_{B-1}, V_{B-2},...,V_1. The total unitary transformation is $V_{\mathcal{B}_1} = V_{B-1}V_{B-2}\cdots V_1$. Acting this on Green's function G yields the transformed Green's function $V^\dagger_{\mathcal{B}_1} G V_{\mathcal{B}_1}$ with $n_1 \approx 0$ or 1. The procedure is repeated for sites 2,...$B+1$ to obtain $V_{\mathcal{B}_2}$. For the last few sites, the block size becomes the number of the remaining sites. In the end we obtain the total unitary transformation $V = V_{\mathcal{B}_1} V_{\mathcal{B}_2} \cdots V_{\mathcal{B}_{N-1}}$.

APPENDIX C: VARIATIONAL CIRCUIT ARCHITECTURES

This subsection details the architecture for the variational circuits shown in Fig. 2. This includes two types of GMPS+X circuits that augment the GMPS Hartree-Fock circuit with additional variational circuits:

(i) the GMPS+J ansatz (where "H" stands for "Heisenberg") depicted in Fig. 2(a) geared towards large-U and half-filling, and
(ii) the GMPS+U ansatz [Fig. 2(b)], which is agnostic to filling and U (although it tends to perform best at large or small U), and
(iii) a problem-agnostic brick circuit [Fig. 2(c)], which can achieve high accuracy, but at the cost of introducing a comparatively large number of variational parameters.

1. GMPS+J

The GMPS+J ansatz exploits the physical picture that the half-filled Fermi-Hubbard model behaves like a Heisenberg spin chain at large Us, by introducing a variational "pre-entangling" circuit before the GMPS circuitry [Fig. 2(a)] using a single extra bond qubit and layer of variational gates to build in quantum fluctuations of the AFM spin texture in the Hartree-Fock ground state. The aim is to emulate a QMPS state of the electron spins without altering the charge state. In our approach, we encode each spinful fermion site into two qubits whose computational basis encodes the particle occupation number of the up and down spin orbitals: $|n_\uparrow, n_\downarrow\rangle$. The input state to the GMPS circuit is simply a product state of Fermi-Hubbard sites with a single particle on each site, and with spin alternating between up and down. To entangle the spin degrees of freedom on different sites without affecting their charge, we employ a basis transformation using a CNOT gate, which corresponds to the following map:

$$\begin{aligned} |n_\uparrow, n_\downarrow\rangle &\longrightarrow |\text{flavor}, 2P_F - 1\rangle : \\ |0,0\rangle &\longrightarrow |0,0\rangle \\ |0,1\rangle &\longrightarrow |0,1\rangle \\ |1,0\rangle &\longrightarrow |1,1\rangle \\ |1,1\rangle &\longrightarrow |1,0\rangle. \end{aligned} \tag{C1}$$

In the transformed basis the second qubit encodes the even and odd fermion parity $P_F = (-1)^{n_\uparrow + n_\downarrow}$. The flavor qubit's interpretation depends on the value of P_F. When P_F is odd, there is a single electron per site and the first qubit's Pauli operators correspond to the electron spin operator, e.g., $Z_1 = c^\dagger_s \sigma^z_{ss'} c_{s'}$ (and similarly for Y, Z). While our initial states always have odd fermion parity, for completeness, we mention that for even fermion parity the "flavor" qubit encodes the occupation number of a spin-singlet Cooper pair created by $c^\dagger_\uparrow c^\dagger_\downarrow$.

In the flavor and parity basis, the electron spin on each site now maps to the state of a single qubit, and we can apply a variational $XX + YY$ gate

$$u_{XX+YY}(\theta) = \exp\left[-i\frac{\theta}{2}(X \otimes X + Y \otimes Y)\right] \tag{C2}$$

between this flavor qubit and an extra bond qubit, emulating the variational circuitry for a QMPS approximation to the Heisenberg spin-chain ground state explored in Ref. [7]. We then transform back to the original particle occupancy basis to implement the GMPS circuit for the Hartree-Fock ground state. The GMPS+J circuit introduces only a single extra variational parameter per site.

2. Brick circuit QMPS

Besides the GMPS+X approaches, we also employ a problem-agnostic variational circuit approach, which we label by the term brick QMPS. Specifically, we fix a brickwork circuit architecture with general particle-number conserving two-qubit gates (see Fig. 2) to generate the tensors of a QMPS with $\chi = 2^4$ and classically minimize $\langle H_{\text{FH}}\rangle$ with respect to the variational parameters using quimb [33]. The number of bond qubits and gates in this ansatz can be arbitrarily scaled to achieve larger expressiveness. However, this introduces a large number of variational parameters (five parameters per two-qubit gate), which may be difficult to train on larger problem instances (e.g., 2D models).

Our brickwork circuit ansatz employs general particle number-conserving two-qubit gates to enable noise mitigation based on postselecting the data on having the correct

TABLE I. Total shots for different measurements ($i = 1, 2, 3$ for $1/3$-filling states and $i = 1, 2$ for $1/2$-filling states), success rate defines the proportional of total shots kept after the noise-mitigation postselection.

Terms:		$c^\dagger_{\uparrow 0}c_{\uparrow 1}$	$c^\dagger_{\downarrow 0}c_{\downarrow 1}$	$c^\dagger_{\uparrow 1}c_{\uparrow 2}$	$c^\dagger_{\downarrow 1}c_{\downarrow 2}$	$c^\dagger_{\uparrow 2}c_{\uparrow 3}$	$c^\dagger_{\downarrow 2}c_{\downarrow 3}$	$n_{i\uparrow}n_{i\downarrow}$	
U	ν	Total shots							Success rate
6	$1/2$	400	400	400	400			1000	58.5%
4	$1/2$	1000	1000					1000	66.4%
1	$1/2$	400	400	400	400			1000	42.1%
6	$1/3$	800	800	800	800	600	800	1000	42.1%
4	$1/3$	800	800	1000	1000	1000	1000	1000	39.1%
1	$1/3$	800	1000	800	1200	1000	1000	1000	29.8%

total particle number, with unitary:

$$U_{2q}(\gamma,\phi,\zeta,\chi,\theta) = \begin{pmatrix} e^{i(\gamma+\phi)} & 0 & 0 & 0 \\ 0 & e^{i(-\gamma+\phi+\zeta)}\sin\theta & e^{-i(\chi+\gamma+\phi)}\cos\theta & 0 \\ 0 & e^{i(\chi-\gamma+\phi)}\cos\theta & e^{-i(\gamma+\phi+\zeta)}\sin\theta & 0 \\ 0 & 0 & 0 & e^{i(\gamma-\phi)} \end{pmatrix}, \tag{C3}$$

where $(\gamma,\phi,\zeta,\chi,\theta)$ are variational parameters [independently chosen for each two-qubit gate in Fig. 2(c)].

APPENDIX D: ERROR MITIGATION

As a simple noise-mitigation method, we postselect our data on having the correct total particle number. Since a noiseless implementation of the circuits conserves total particle number, any deviation from the ideal number can only be caused by gate errors (though not vice versa). This symmetry-based postselection gives a modest but noticeable improvement in measuring Green's functions and density correlations. An example is shown in Fig. 8, comparing the measurement results with and without the noise mitigation.

When all the measurements are in the Pauli-Z bases, it is convenient to keep track of the particle number just using the measurement results. The most straightforward way of measuring Green's functions $\langle c^\dagger_{r_1}c_{r_2}\rangle$, would be to implement separate measurements of its real and imaginary parts as Pauli strings: "$...XZ...Z...ZX...$" and "$...YZ...Z...ZY...$". However, as these strings do not individually commute with total particle number, the method would be incompatible with our error-mitigation scheme. Instead, we add additional gates to map $X_iX_j + Y_iY_j$ and $Z_i + Z_j$ eigenstates to the computational basis so that the real part of G and the total number can be simultaneously measured. This mapping is achieved by the unitary (written in the Z_i, Z_j eigenbasis):

$$U_M = \begin{pmatrix} 1 & 0 & 0 & 0 \\ 0 & \frac{1}{\sqrt{2}} & \frac{1}{\sqrt{2}} & 0 \\ 0 & \frac{1}{\sqrt{2}} & -\frac{1}{\sqrt{2}} & 0 \\ 0 & 0 & 0 & 1 \end{pmatrix}. \tag{D1}$$

Since the state is built sequentially from left to right, performing this rotation requires postponing the mid-circuit measurement and resetting the qubit at r_1 until site r_2 is reached, which requires a single extra hardware qubit compared to the basic QMPS circuit without error mitigation.

APPENDIX E: GMPS FOR SUPERCONDUCTORS AND THERMAL STATES

While Ref. [15] focused on the classical GMPS method for ground states of real, number-conserving free-fermion Hamiltonians, it is straightforward to generalize this framework to general Gaussian fermion pure and mixed states. The case of complex Hamiltonian entries is already accounted for by the phases, ϕ in Eq. (B1) above. Below we briefly sketch the generalizations for superconducting and mixed (e.g., thermal) Gaussian states.

1. Particle non-conserving states (superconductors)

For superconducting mean-field states that do not conserve particle number, a standard convenient trick is to redundantly represent N fermion orbitals using a $2N$-component Nambu operator:

$$\psi_{i,s} = \left(c_1, \quad \ldots c_N, \quad c_1^\dagger, \quad \ldots \quad c_N^\dagger\right)^T, \tag{E1}$$

where $s = +1$ corresponds to the particle (c_i) block and $s = -1$ to the hole ($c_i^\dagger$) block. Denoting the Pauli matrices in this particle-hole space as $\vec{\tau}_{ss'}$, this description has a particle-hole redundancy $\psi^\dagger = \tau^1\psi$. The classical part of the GMPS algorithm can then be run as normal in this Nambu basis, except that each time one identifies an approximate block eigenvector $\mathbf{v}$ with block occupation number n close to 0 or 1, its particle-hole conjugate $\tau^1\vec{v}$

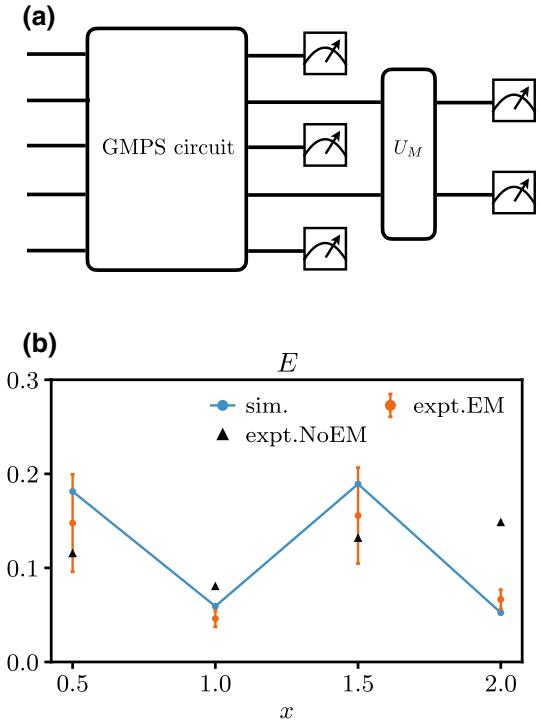

FIG. 8. Error mitigation. (a) To mitigate hardware errors, we postselect on results with the correct total particle number. To simultaneously measure total particle number and Green's function elements $\langle c_i^\dagger c_j \rangle$, we add a basis transformation gate U_M for the corresponding qubits of Green's functions before measuring them and each qubit is measured in the Pauli-Z basis as in Ref. [20]. In the holographic implementation, the first qubit being measured cannot be reset and reused until both sites i,j are measured. (b) A comparison between measurement results for the QMPS VQE method of $U = 6$, half-filled Fermi-Hubbard model with (EM) and without (NoEM) the error mitigation. Details of postselection success rate and shot counts are shown in Table I.

will also be a block eigenvector with the block occupation number $1 - n$, which is equally well localized to the block. These vectors should be simultaneously decoupled from the rest of the system by implementing rotations V_B and $\tau^1 V_B \tau^1$ on G. In the many-body language the many-body operator corresponding to single-particle rotation V_{ij} is $e^{\psi_{is}^\dagger (\log V)_{is,js'} \psi_{js}}$, which will automatically perform both V_B and $\tau^1 V_B \tau^1$ rotations due to the particle-hole redundancy.

2. Thermal states via purifications

It is also possible to prepare a purified version of Gaussian mixed states via GMPS methods at the cost of doubling the number of qubits required compared to a pure Gaussian state. Without loss of generality, we consider this method for thermal states of the form: $\rho = (1/Z)e^{-c_i^\dagger h_{ij} c_j}$ (where we have chosen normalization of h such that temperature is 1, and Z normalizes $\mathrm{tr}\rho = 1$), since any Gaussian mixed state can be represented in this way. We expect the compression to be effective when h is a local Hamiltonian, since these thermal states will have an area-law scaling of mutual information [34] and efficient matrix-product density operator form [35].

The basic idea is to prepare a thermofield-double- (TFD) type state on a doubled system with the fermion creation operators of the system and double respectively labeled as c_i, a_i (here "a" stands for ancilla). To start, consider just a single-mode thermal state $\rho_T = (1/Z)e^{-\varepsilon c^\dagger c}$. This can be prepared as a TFD state: $|\Psi_{\mathrm{TFD}}\rangle = (1/\sqrt{Z})e^{-\varepsilon c^\dagger a/2}|0\rangle_s \otimes |1\rangle_a$, which has the properties (i) $\rho_T = \mathrm{tr}_a |\Psi_{\mathrm{TFD}}\rangle\langle\Psi_{\mathrm{TFD}}|$, and (ii) $|\Psi_{\mathrm{TFD}}\rangle$ is a Gaussian fermion state that can be approximately prepared as a GMPS acting on the doubled $\{c, a\}$ system. For multiple modes, this simply generalizes to $|\Psi_{\mathrm{TFD}}\rangle = (1/\sqrt{Z})e^{-c_i^\dagger h_{ij} a_j}|0\rangle_s \otimes |1\rangle_a$ where $|0\rangle$ is the all-empty state, and $|1\rangle$ is the all-full state, respectively, (as can be seen by working in the eigenbasis of h_{ij}, which reduces to the single-mode problem above).

This Gaussian TFD (GTFD) preparation could be particularly effective as a starting point for variational thermal state-preparation schemes based on minimizing the free energy $F = \langle H \rangle - TS$ where $S = -\mathrm{tr}\rho_s \log \rho_s$. Namely, whereas computation of $\langle H \rangle$ for a variational state is straightforward on a quantum computer, measurements of S for an unknown state incur exponential sampling overhead [36,37]. However, if one starts with a GTFD state, and adds subsequent variational circuit layers acting on the c system alone, the entropy of the c system remains that of the initial thermal state, which can be efficiently calculated classically. The resulting state has a fine-tuned entanglement spectrum that is the direct product of many independent two-state systems (one per fermion orbital). Generic thermal states instead exhibit random-matrix-type entanglement spectrum with level repulsion between nearby entanglement energies. However, recent work [38] provides evidence and arguments that the fine details of the entanglement level spacing statistics are not visible in physical quantities of interest such as correlations of local observables and that product-state entanglement spectrum ansatzes are effective at reproducing such observables in correlated thermal states.

APPENDIX F: CIRCUMVENTING JORDAN-WIGNER STRING MEASUREMENTS

Measuring fermion correlations between distant sites requires measuring long Jordan-Wigner strings. Errors in measurement will generically cause such observables to decay exponentially in distance. While this effect is minor for moderate system sizes explored in this paper, it may become a dominant source of error in larger-scale models. Here, we show that in holographic QMPS simulations, it is possible to avoid the measurement of long JW strings, by "pulling" the strings back into the virtual bond space

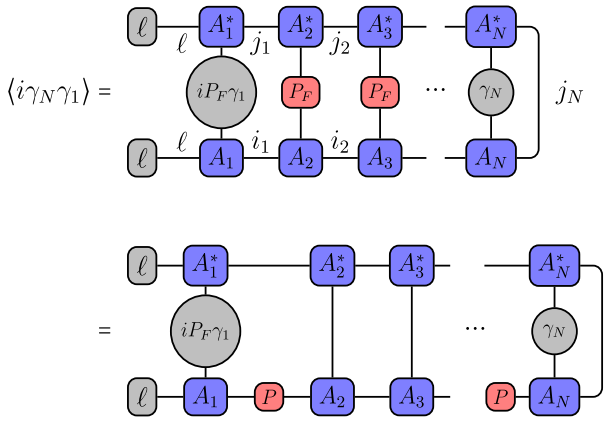

FIG. 9. Schematic representation of applying Eq. (B1) to fermionic operator $\gamma_{1,N}$.

of the MPS (see Appendix A of Ref. [39]) where they largely cancel except for additional boundary terms that can be measured by sampling results from a small number of different QMPS contractions.

The measurement of a Jordan-Wigner string can be simplified in the following way: first, we pull back the Jordan-Wigner strings onto the bond space. Specifically, for tensors that have definite fermion parity, it is always possible to pull back the action of fermion parity operators: $P_{F,i} = (-1)^{n_{F,i}}$ where $n_{F,i}$ is the total number of physical fermions on site i, which appears in the JW string, into operators acting on the input and output bonds of the tensor:

$$(P_F)_s A_s^{ij} = P_{ik}^{\dagger} A_s^{ij} P_{lj}, \tag{F1}$$

where P is the representation of fermion parity on the bond space. Crucially, each bond in the middle of the JW string has a P from the tensor to its left and a $P^{\dagger}$ from the tensor to its right, which cancel, leaving only Ps at the terminal bonds, as shown schematically in Fig. 9.

The transfer matrix with P acting on the lower leg but not the upper leg is not a valid quantum channel, but we can decompose it as a linear combination of a small number of quantum channels that can be separately measured, and then linearly combined to compute the desired result. To this end, we introduce the following two basic operations on the bond space. First, denote measurement of bond-fermion parity M_P:

$$\begin{aligned} M_P &= \Pi_{P=1} \otimes \Pi_{P=1} - \Pi_{P=-1} \otimes \Pi_{P=-1} \\ &= \frac{(1+P)}{2} \otimes \frac{(1+P)}{2} - \frac{(1-P)}{2} \otimes \frac{(1-P)}{2} \\ &= \frac{1}{2}\left[P \otimes 1 + 1 \otimes P\right]. \end{aligned} \tag{F2}$$

Implementing M_P requires measuring P on the bond register without collapsing the full bond-wave function, which in practice can be done using an ancilla and standard phase-kickback scheme (one of the physical qubits, which has already been measured and is currently not active can play this role so that the total qubit resource requirements are unaffected).

Second, we define the operator $\sin((\pi/4)\mathrm{ad}_P)$ where $\mathrm{ad}_P \circ = [P, \circ]$:

$$\begin{aligned} \sin\left(\frac{\pi}{4}\mathrm{ad}_P\right) &= \frac{1}{2i}\left(e^{i\frac{\pi}{4}\mathrm{ad}_P} - e^{-i\frac{\pi}{4}\mathrm{ad}_P}\right) \\ &= \frac{1}{2}\left(P \otimes 1 - 1 \otimes P\right), \end{aligned} \tag{F3}$$

and each of the terms: $e^{i(\pi/4)\mathrm{ad}_P} = e^{\pm i\pi P/4} \otimes e^{\mp i\pi P/4}$ can be implemented simply by applying the unitary operator $e^{\pm i\pi P/4}$ to the bond-qubit register.

From these two ingredients, the desired operation of applying P to the lower bond legs but not the upper ones can then be written as

$$P \otimes 1 = M_P + \frac{1}{2i}\left(e^{i\pi P/4} \otimes e^{-i\pi P/4} - e^{-i\pi P/4} \otimes e^{i\pi P/4}\right), \tag{F4}$$

which we have just shown can be expressed as a weighted sum of the results obtained by sampling four different valid quantum channels that can each be implemented holographically.

This method becomes useful in cases where mid-circuit measurement errors are the dominant source of error (as opposed to, say, gate errors building up in the implementation of the QMPS tensors), and becomes helpful when the JW string is sufficiently long that its measurement error exceeds that introduced by the extra circuitry required to perform the M_P and $\sin(\pi/4\mathrm{ad}_P)$ operations.

APPENDIX G: ADDITIONAL DATA FOR BRICK QMPS

In this section, we present additional simulation and experimental data for the problem-agnostic brick circuit QMPS for the Fermi-Hubbard chain at half-filling and 1/3-filling in Fig. 10. Noiseless simulations of the problem-agnostic brick-circuit QMPS approach show that it can effectively capture the ground state and correlations over a range of U and filling factors. To minimize the impact of errors, and reduce the implementation time for experimental demonstrations of this brick circuit QMPS, we first classically optimize the circuit parameters to minimize the variational energy for an infinite MPS (IMPS). From this, we classically compute the steady state of the bond-transfer matrix and synthesize a circuit acting on the bond qubits and one ancilla, which approximately prepares this steady state. This circuit is then used to prepare an initial mixed state of the bond qubits, which closely approximates their bulk steady state, allowing us to directly access

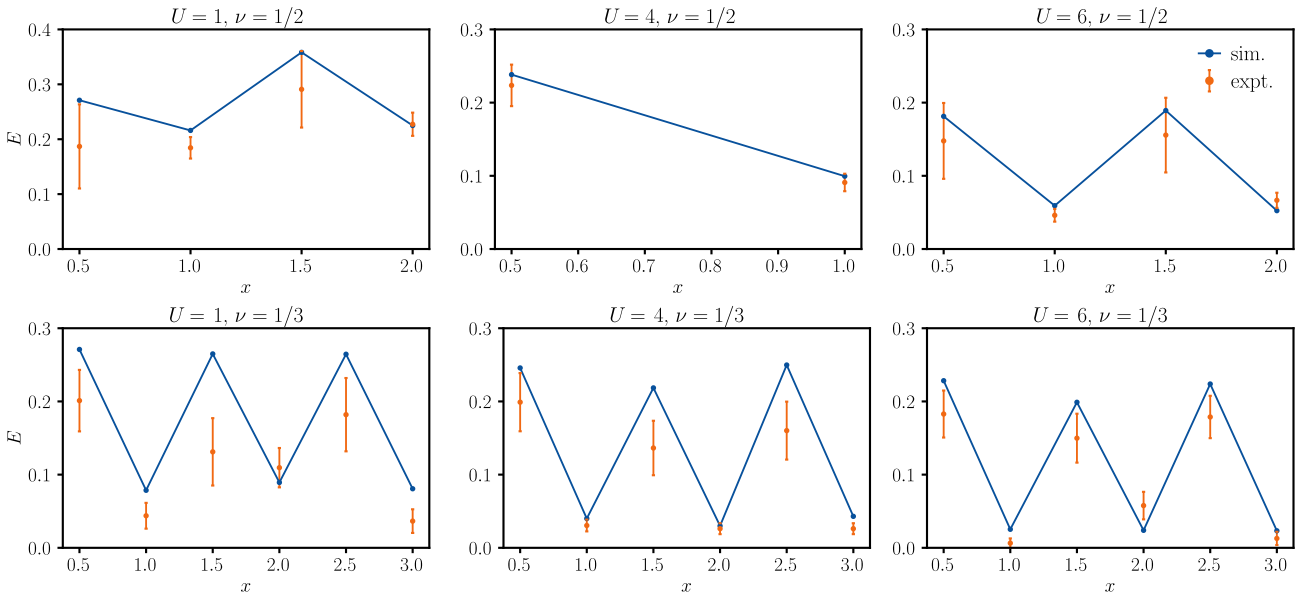

FIG. 10. Brick QMPS method measurement data of Green's functions and density correlations of the Fermi-Hubbard model of different Us and fillings. Absolute value of hopping energies $t\langle\frac{1}{2}(c^\dagger_{i\uparrow}c_{i+1\uparrow} + c^\dagger_{i\downarrow}c_{i+1\downarrow})\rangle$ are shown at bond-centered coordinates with half-integer positions $x = i - 0.5$, where i labels the spinful sites. On-site repulsion density correlations $\langle n_{i\uparrow}n_{i\downarrow}\rangle$ are shown at site-centered coordinates (integer i).

the infinite system-size limit without iteratively "burning in" the bond channel as previously done in Ref. [7]. We note that a similar technique was employed by Ref. [6]. We emphasize that this technique is only viable for small problem sizes where classical simulations are tractable. This, however, may still be useful for preparing, say, a moderate bond-dimension approximation of a correlated ground state, which is subsequently subjected to rapidly entangling time evolution that could not be simulated classically.

The experimental data agrees well at larger values of U but deviates significantly at $U = 1$. Since the charge correlation length increases with smaller Us, we interpret these deviations as arising from increased propagation of noise and errors in large-correlation length QMPS.

[1] F. Arute, K. Arya, R. Babbush, D. Bacon, J. Bardin, R. Barends, R. Biswas, S. Boixo, F. Brandao, D. Buell, B. Burkett, Y. Chen, Z. Chen, B. Chiaro, R. Collins, W. Courtney, A. Dunsworth, E. Farhi, B. Foxen, and J. Martinis, Quantum supremacy using a programmable superconducting processor, Nature **574**, 505 (2019).

[2] H.-S. Zhong, H. Wang, Y.-H. Deng, M.-C. Chen, L.-C. Peng, Y.-H. Luo, J. Qin, D. Wu, X. Ding, Y. Hu *et al.*, Quantum computational advantage using photons, Science **370**, 1460 (2020).

[3] S. Aaronson and A. Arkhipov, in *Proceedings of the forty-third annual ACM symposium on Theory of computing* (2011), p. 333.

[4] B. Bauer, S. Bravyi, M. Motta, and G. K.-L. Chan, Quantum algorithms for quantum chemistry and quantum materials science, Chem. Rev. **120**, 12685 (2020).

[5] U. Schollwöck, The density-matrix renormalization group in the age of matrix product states, Ann. Phys. (N. Y) **326**, 96 (2011).

[6] F. Barratt, J. Dborin, M. Bal, V. Stojevic, F. Pollmann, and A. Green, Parallel quantum simulation of large systems on small NISQ computers, Npj Quantum Inf. **7**, 1 (2021).

[7] M. Foss-Feig, D. Hayes, J. M. Dreiling, C. Figgatt, J. P. Gaebler, S. A. Moses, J. M. Pino, and A. C. Potter, Holographic quantum algorithms for simulating correlated spin systems, Phys. Rev. Res. **3**, 033002 (2021).

[8] S.-H. Lin, R. Dilip, A. G. Green, A. Smith, and F. Pollmann, Real- and Imaginary-Time Evolution with Compressed Quantum Circuits, PRX Quantum **2**, 010342 (2021).

[9] M. Foss-Feig, S. Ragole, A. Potter, J. Dreiling, C. Figgatt, J. Gaebler, A. Hall, S. Moses, J. Pino, B. Spaun *et al.*, Entanglement from tensor networks on a trapped-ion QCCD quantum computer, arXiv preprint arXiv:2104.11235 (2021).

[10] E. Chertkov, J. Bohnet, D. Francois, J. Gaebler, D. Gresh, A. Hankin, K. Lee, R. Tobey, D. Hayes, B. Neyenhuis *et al.*, Holographic dynamics simulations with a trapped ion quantum computer, arXiv preprint arXiv:2105.09324 (2021).

[11] L. Slattery and B. K. Clark, Quantum circuits for two-dimensional isometric tensor networks, arXiv preprint arXiv:2108.02792 (2021).

[12] I. MacCormack, A. Galda, and A. L. Lyon, Simulating large PEPs tensor networks on small quantum devices, arXiv preprint arXiv:2110.00507 (2021).

[13] Y. Zhang, S. Jahanbani, D. Niu, R. Haghshenas, and A. C. Potter, Qubit-efficient simulation of thermal states with quantum tensor networks, arXiv preprint arXiv:2205.06299 (2022).

[14] I. H. Kim, Holographic quantum simulation, arXiv preprint arXiv:1702.02093 (2017).

[15] M. T. Fishman and S. R. White, Compression of correlation matrices and an efficient method for forming matrix product states of fermionic Gaussian states, Phys. Rev. B **92**, 075132 (2015).

[16] D. Perez-Garcia, F. Verstraete, M. M. Wolf, and J. I. Cirac, Matrix product state representations, arXiv preprint arXiv:quant-ph/0608197 (2006).

[17] L. Gyongyosi and S. Imre, Properties of the quantum channel, arXiv preprint arXiv:1208.1270 (2012).

[18] In the last step, there is no reason to continue the chain beyond site $x = L$ where L is the rightmost site where the observable has support: since we are preparing a state in RCF, the tensor contractions without operator insertions for $x > L$ simply multiply the $x \leq L$ network from the right by the identity vector, which corresponds to tracing out or discarding the bond qubits.

[19] I. D. Kivlichan, J. McClean, N. Wiebe, C. Gidney, A. Aspuru-Guzik, G. K.-L. Chan, and R. Babbush, Quantum Simulation of Electronic Structure with Linear Depth and Connectivity, Phys. Rev. Lett. **120**, 110501 (2018).

[20] F. Arute K. Arya, R. Babbush, D. Bacon, J. C. Bardin, R. Barends, S. Boixo, M. Broughton, B. B. Buckley, D. A. Buell *et al.*, Hartree-Fock on a superconducting qubit quantum computer, Science **369**, 1084 (2020).

[21] We note that these asymptotic expressions are asymptotic in L and assume nonzero density of particles. For finite-size molecules there may be individual orbitals that add extra overhead.

[22] A general $SU(4)$ unitary has 15 variational parameters, this can be reduced to 5 by enforcing symmetry and exploiting the gauge structure of the matrix-product states.

[23] T. Neupert, L. Santos, C. Chamon, and C. Mudry, Fractional Quantum Hall States at Zero Magnetic Field, Phys. Rev. Lett. **106**, 236804 (2011).

[24] M. B. Hastings and X.-G. Wen, Quasiadiabatic continuation of quantum states: The stability of topological ground-state degeneracy and emergent gauge invariance, Phys. Rev. B **72**, 045141 (2005).

[25] S. Lloyd, Universal quantum simulators, Science **273**, 1073 (1996).

[26] A. M. Childs, Y. Su, M. C. Tran, N. Wiebe, and S. Zhu, Theory of Trotter Error with Commutator Scaling, Phys. Rev. X **11**, 011020 (2021).

[27] These gate count scalings are for *local* quasiadiabatic preparation [24] sufficient to accurately reproduce correlations of local operators, true adiabatic preparation to produce full many-body state fidelity close to 1 requires a multiplicative factor of L^2.

[28] We note that the gate count gains are asymptotic, for the task of simulating a spinful $L_x = 8$ FH chain, both methods require nearly the same number of entangling gates (130 Mølmer-Sørensen gates for GMPS versus 128 $\sqrt{\text{iSWAP}}$ gates for given rotations). For any $L_x > 8$, the GMPS approach requires fewer gates.

[29] A. J. Ferris, Fourier Transform for Fermionic Systems and the Spectral Tensor Network, Phys. Rev. Lett. **113**, 010401 (2014).

[30] R. Haghshenas, J. Gray, A. C. Potter, and G. K.-L. Chan, The variational power of quantum circuit tensor networks, arXiv:2107.01307 [quant-ph] (2021).

[31] I. H. Kim and B. Swingle, Robust entanglement renormalization on a noisy quantum computer, arXiv preprint arXiv:1711.07500 (2017).

[32] J. M. Pino, J. M. Dreiling, C. Figgatt, J. P. Gaebler, S. A. Moses, M. Allman, C. Baldwin, M. Foss-Feig, D. Hayes, K. Mayer, C. Ryan-Anderson, and B. Neyenhuis, Demonstration of the trapped-ion quantum CCD computer architecture, Nature **592**, 209 (2021).

[33] J. Gray, quimb: A python library for quantum information and many-body calculations, J. Open Source Softw. **3**, 819 (2018).

[34] M. M. Wolf, F. Verstraete, M. B. Hastings, and J. I. Cirac, Area Laws in Quantum Systems: Mutual Information and Correlations, Phys. Rev. Lett. **100**, 070502 (2008).

[35] J. G. Jarkovskỳ, A. Molnár, N. Schuch, and J. I. Cirac, Efficient Description of Many-Body Systems with Matrix Product Density Operators, PRX Quantum **1**, 010304 (2020).

[36] R. Islam, R. Ma, P. M. Preiss, M. E. Tai, A. Lukin, M. Rispoli, and M. Greiner, Measuring entanglement entropy in a quantum many-body system, Nature **528**, 77 (2015).

[37] T. Brydges, A. Elben, P. Jurcevic, B. Vermersch, C. Maier, B. P. Lanyon, P. Zoller, R. Blatt, and C. F. Roos, Probing Rényi entanglement entropy via randomized measurements, Science **364**, 260 (2019).

[38] J. Martyn and B. Swingle, Product spectrum ansatz and the simplicity of thermal states, Phys. Rev. A **100**, 032107 (2019).

[39] P. Corboz and G. Vidal, Fermionic multiscale entanglement renormalization ansatz, Phys. Rev. B **80**, 165129 (2009).